ADVANCES IN ATMOSPHERIC SCIENCES, VOL. 30, NO. 6, 2013, 1758–1770

Why Does FGOALS-gl Reproduce a Weak Medieval Warm Period But a Reasonable Little Ice Age and 20th Century Warming?

GUO Zhun (郭 准)[1,2] and ZHOU Tianjun (周天军)*[1]

[1] *State Key Laboratory of Numerical Modeling for Atmospheric Sciences and Geophysical Fluid Dynamics, Institute of Atmospheric Physics, Chinese Academy of Sciences, Beijing* 100029

[2] *Climate Change Research Center, Chinese Academy of Sciences, Beijing* 100029

(Received 16 September 2012; revised 25 February 2013; accepted 27 Febuary 2013)

ABSTRACT

To understand the strengths and limitations of a low-resolution version of Flexible Global Ocean–Atmosphere–Land–Sea-ice (FGOALS-gl) to simulate the climate of the last millennium, the energy balance, climate sensitivity and absorption feedback of the model are analyzed. Simulation of last-millennium climate was carried out by driving the model with natural (solar radiation and volcanic eruptions) and anthropogenic (greenhouse gases and aerosols) forcing agents. The model feedback factors for (model sensitivity to) different forcings were calculated. The results show that the system feedback factor is about 2.5 (W m^{-2}) K^{-1} in the pre-industrial period, while 1.9 (W m^{-2}) K^{-1} in the industrial era. Thus, the model's sensitivity to natural forcing is weak, which explains why it reproduces a weak Medieval Warm Period. The relatively reasonable simulation of the Little Ice Age is caused by both the specified radiative forcing and unforced linear cold drift. The model sensitivity in the industrial era is higher than that of the pre-industrial period. A negative net cloud radiative feedback operates during whole-millennial simulation and reduces the model's sensitivity to specified forcing. The negative net cloud radiative forcing feedback under natural forcing in the period prior to 1850 is due to the underestimation (overestimation) of the response of cloudiness (in-cloud water path). In the industrial era, the strong tropospheric temperature response enlarges the effective radius of ice clouds and reduces the fractional ice content within cloud, resulting in a weak negative net cloud feedback in the industrial period. The water vapor feedback in the industrial era is also stronger than that in the pre-industrial period. Both are in favor of higher model sensitivity and thus a reasonable simulation of the 20th century global warming.

Key words: millennial climate simulation, climate sensitivity, feedback, cloud, water vapor

Citation: Guo, Z., and T. J. Zhou, 2013: Why does FGOALS-gl reproduce a weak Medieval Warm Period but a reasonable Little Ice Age and 20th century warming? *Adv. Atmos. Sci.*, **30**(6), 1758–1770, doi: 10.1007/s00376-013-2227-8.

1. Introduction

To understand the evolution of the Earth's climate, simulation of the climate of the last millenium has been a hot topic of the climate modeling community in recent decade. In the recent design of Coupled Model Intercomparison Project Phase 5 (CMIP5) standard experiments, last-millennium climate simulation is on the list of long-term experiments (Taylor et al., 2012). However, how to reasonably simulate last-millennium climate remains a challenge. For example, even when forced by identical external forcing agents including solar variation, volcanic eruptions, and internal forcing agents including greenhouse gases and aerosols, different models generate different results (Jansen et al., 2007). Understanding this issue is of crucial importance to the climate modeling community.

Essentially, last-millennium climate simulation is the response of a coupled system to the specified external and internal forcings. A reliable response depends on the model's sensitivity to the specified forcing agents. Climate sensitivity and radiative forcing are useful measures of model sensitivity (Houghton et al., 2001). Surface air temperature (SAT) response is

*Corresponding author: ZHOU Tianjun, zhoutj@lasg.iap.ac.cn

a criterion to quantify climate sensitivity. The SAT response and climate sensitivity to external and internal forcing are determined by the physical processes and feedbacks, including cloud, ice, water vapor, and so on (Cess et al., 1990; Houghton et al., 1990; Cess et al., 1996; Colman, 2003). A model's climate sensitivity is related to the uncertainties regarding how clouds and other elements of the climate system feed back on SAT changes (Forster and Taylor, 2006). Among the physical processes, positive water vapor feedback is a well-known positive feedback mechanism to increase the climate sensitivity of the model (e.g., Manabe and Wetherald, 1967; Held and Soden, 2000, 2006), in which warmer conditions provide more water vapor, which amplifies the initial warming as greenhouse gas (GHG). This positive water vapor feedback in climate models is about 2.2 W m^{-2} K^{-1} (Cess et al., 1990). Compared to water vapor feedback, cloud feedback is more complex and plays a key role in determining the sensitivity of model climate to internal and external forcing (Cess et al., 1990; Zhang et al., 1994). For example, if global cloudiness decreases because of warming, like many climate models have shown, it will reduce the infrared greenhouse effect of cloud. In this hypothesis, cloud acts as a negative longwave feedback mechanism because the infrared radiation emits more efficiently. Meanwhile, the decreasing cloudiness also leads to a positive feedback mechanism by reducing solar reflection. These effects complicate the cloud feedback processes. If the effects of cloud optical properties and vertical structure were considered, the feedback would be even more complex (Cess and Potter, 1988). Since different climate models usually differ in the cloud schemes employed, their climate sensitivities are also different.

The evolution of last-millennial climate includes three typical periods: the Medieval Warm Period (MWP) from 1000 A.D. to 1340 A.D., the Little Ice Age (LIA) from 1400 A.D. to 1850 A.D., and the 20th century global warming. As shown in Fig. 1a, millennial climate simulation by Flexible Global Ocean–Atmosphere–Land–Sea-ice (FGOALS-gl) model is generally in good agreement with the reconstruction in SAT evolution, especially for the cooling of the LIA. The model also reasonably simulates the main characteristics of temperature change in the 20th century, especially at global, hemispheric, and continental scales (Zhang et al., 2009; Man et al., 2010a, b). However, the simulated MWP is weaker than the reconstruction. The reasons for the weaker MWP but reasonable LIA and 20th century warming remain unknown. Therefore, the main motivation of this study was to try to understand this issue from the perspective of model sensitivity to external and internal forcing agents. We examine the model's sensitivity to external forcing during the pre-industrial period and compare it to that during the industrial period, i.e., the 20th century. The physical processes that affect model sensitivity are discussed. We present evidence that the weak reproduction of the MWP is due to weak model sensitivity to the specified natural forcing agents in the pre-industrial period. Both the negative cloud feedback and weak positive water vapor feedback reduce the climate sensitivity of the model. In the industrial era, however, because the cloud radiative feedback is weak, while the positive water vapor feedback is strong, the higher-than-preindustrial-period model sensitivity leads to a reasonable simulation of the 20th century warming.

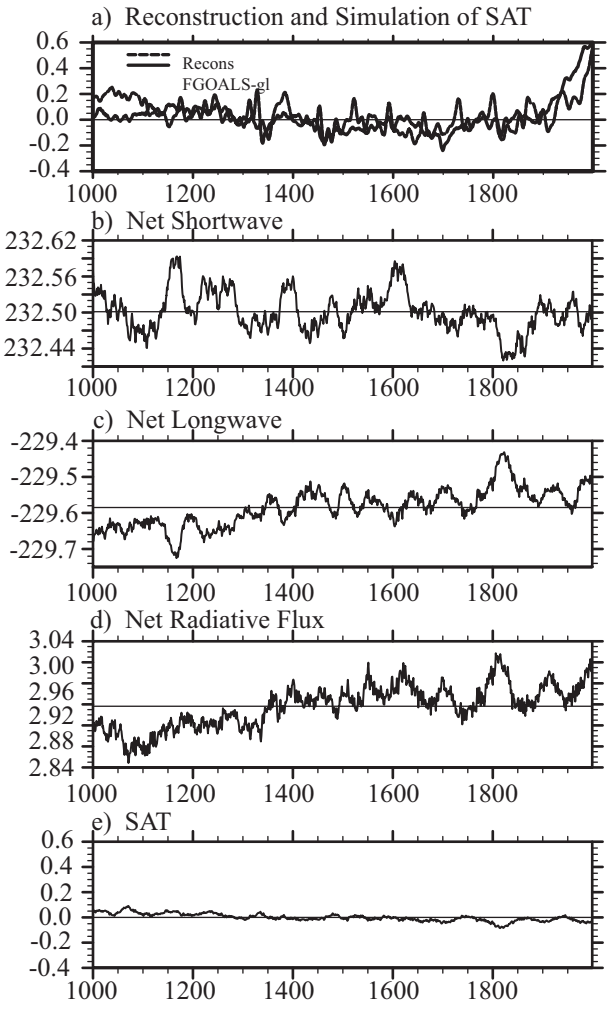

Fig. 1. (a) Reconstruction and simulation of the unforced global mean SAT; (b) net shortwave flux (downward is positive; units: W m^{-2}) at TOA; (c) net longwave flux (downward is positive; units: W m^{-2}) at TOA; (d) net radiative flux (downward is positive; units: W m^{-2}) at TOA; and (e) SAT (units: K).

The remainder of this paper is organized as follows. The model, data and methodology are described in section 2. In section 3, we answer the following questions: (1) How sensitive is FGOALS-gl in its response to external and internal forcing agents? (2) Does the model have different sensitivity to different forcing agents? (3) How do cloud properties and water vapor responses impact the climate sensitivity of the model? The major findings are then summarized in section 4.

2. Model, data and method

2.1 *Model description and cloud radiation schemes*

The fast version of the LASG/IAP(State Key Laboratory of Numerical Modeling for Atmospheric Sciences and Geophysical Fluid Dynamics/Institute of Atmospheric Physics) FGOALS model was applied in this study. FGOALS is a fully-coupled model that has four individual components, including atmospheric, oceanic, land and sea-ice models, coupled together by the National Center for Atmospheric Research Community Climate System Model (NCAR CCSM2) coupler (Zhou et al., 2008). The atmospheric component of FGOALS is a low-resolution version of the Grid Atmospheric Model of IAP/LASG (GAMIL), and thus this coupled model is referred as "FGOALS-gl". The atmospheric component of FGOALS-gl has an approximate 5° (lon) ×4.5° (lat) horizontal grid and 26 sigma levels in the vertical direction (Wen et al., 2007). In GAMIL, the formulations of the physical parameterizations are transplanted from the NCAR Community Atmosphere Model (CAM2). The LASG/IAP Climate Ocean Model (LICOM), which has a horizontal resolution of 1°×1°, and 30 levels in the vertical direction, is employed as the oceanic component in the fully-coupled model. The other two components of FGOALS-gl, i.e., the sea ice model and land model, are transplanted from the NCAR CCSM2. In FGOALS-gl, during the coupled integration, the correction of freshwater fluxes and heat exchange at the interfaces among the aforementioned four coupled components are not considered. For more details of FGOALS-gl, the reader is referred to Zhou et al. (2008). Previous studies (Zhang et al., 2009; Man et al., 2010a; Man and Zhou, 2011; Zhou et al., 2011) indicate that the climatic characteristics of the 20th century and some other periods of the last millennium are reproduced well by FGOALS-gl.

In FGOALS-gl the radiation effects of cloud are derived from in-cloud water path (CWP), cloud fractions, effective radius and fractional ice content (Slingo, 1989). In the model, the effective radius of cloud is only a function of temperature (Kristjánsson and Kristiansen, 2000; Collins et al., 2003):

$$\tau_{\mathrm{c,i}} = C\left(a_{\mathrm{i},m} + \frac{b_{\mathrm{i},m}}{r_{\mathrm{e,i}}}\right) f_{\mathrm{ice}}\,, \tag{1}$$

$$\tau_{\mathrm{c,l}} = C\left(a_{\mathrm{l},m} + \frac{b_{\mathrm{l},m}}{r_{\mathrm{e,l}}}\right)(1 - f_{\mathrm{ice}})\,, \tag{2}$$

$$\varepsilon_{\mathrm{cld}} = 1 - e^{-D\left[\left(0.005+\frac{1}{r_{\mathrm{e,i}}}\right)f_{\mathrm{ice}}+k_{\mathrm{l}}(1-f_{\mathrm{ice}})\right]C}\,, \tag{3}$$

where $\varepsilon_{\mathrm{cld}}$ is cloud emissivity, k_{l} is the infrared absorption coefficient for liquid cloud water (value of 0.090361), $\tau_{\mathrm{c,i}}$ is ice cloud optical depth, and f_{ice} is fractional ice content. a and b are coefficients for the four pseudo-spectral intervals (m), the subscripts i and l indicate ice and liquid. $r_{\mathrm{e,i}}$ and $r_{\mathrm{e,l}}$ are the effective radius of ice and liquid cloud particles, and D is a diffusivity factor.

2.2 *Experimental design and satellite data*

The outputs of two simulations are analyzed in this paper. The first is a 1000-yr pre-industrial control run, and the second is an all-forcing last-millennium climate simulation. In the last-millennium climate simulation, FGOALS-gl was driven by reconstructed natural (solar activity and volcanic aerosols) and anthropogenic forcings (sulfate aerosols and GHG emissions, including CO_2, CH_4 and N_2O). The former is taken from Crowley (2000), and the latter from Ammann et al. (2007). The forcing data for the 20th century are from the CMIP3 20C3M experiments (Zhou and Yu, 2006). Note that in our experiment, the solar and volcanic forcing agents were treated as effective solar radiation; that is, the sum of incoming solar radiation and the reflected solar radiation of volcanic aerosols. For details of the two experiments, the readers are referred to Zhang (2010) and Man and Zhou (2011).

The observational data used in the analysis include: (1) the Earth Radiation Budget Experiment (ERBE) (Barkstrom and Smith, 1986) data for evaluation of the radiative budget at the top of the atmosphere (TOA); (2) International Satellite Cloud Climatology Project (ISCCP) data spanning the period 1983–2000 A.D. (Doutriaux-Boucher and Sèze, 1998; Zhang et al., 2004) for cloud properties (including cloudiness and CWP) and long-term radiative fluxes; (3) the Clouds and the Earth's Radiant Energy System (CERES; http://ceres.larc.nasa.gov) spanning the period 2001–12; and (4) Reconstruction data from Mann et al. (2009) is a global dataset and used in model comparisons. The data were calibrated using 5.0°×5.0° Climate Research Unit (CRU) gridded temperature data, and thus the methodology resulted in reconstructed gridded temperature fields.

2.3 *Method for measuring climate feedback factor and sensitivities*

With the ever-increasing levels of development and complexity of coupled models, radiative forcing and climate sensitivity become harder to diagnose (Gregory et al., 2004; Forster and Taylor, 2006). Based on Forster and Taylor (2006), the climate feedback factor (Y), which is the inverse of climate sensitivity, can be calculated from

$$N = Q - Y(\Delta T_{\rm s}) \,, \tag{4}$$

where N is the net flux imbalance of the coupled climate system, Q is the radiative forcing at the TOA, and $\Delta T_{\rm s}$ is the globally-averaged surface air temperature change.

Based on previous studies (Gregory et al., 2004; Forster and Gregory, 2006; Forster and Taylor, 2006), we regress $Q-N$ against $\Delta T_{\rm s}$ to get a value for Y from the slope of the regression line.

2.4 *Cloud radiative forcing and water vapor feedback*

The effects of cloud on the global radiative energy balance are measured by the TOA cloud radiative forcing (CRF), which is defined by the difference of clear-sky and all-sky radiative fluxes (Ramanathan et al., 1989). Following Ramanathan et al. (1989) and Harrison et al. (1990), the net CRF, which contains shortwave (SW) and longwave (LW) CRF, is defined as

$$\text{SWCRF} = S_{\rm c} - S \,, \tag{5}$$

$$\text{LWCRF} = \text{OLR}_{\rm c} - \text{OLR} \,, \tag{6}$$

$$\text{NetCRF} = \text{SWCRF} + \text{LWCRF} \,, \tag{7}$$

where S and $S_{\rm c}$ respectively denote the all-sky and clear-sky reflected shortwave fluxes at TOA; and OLR and $\text{OLR}_{\rm c}$ are the TOA all-sky and clear-sky outgoing longwave fluxes, respectively.

Based on Sun et al. (2003), the greenhouse effect of water vapor (GHE) is defined as:

$$\text{GHE} = \sigma(\text{SAT})^4 - \text{OLR}_{\rm c} \,, \tag{8}$$

where σ is the Stefan–Boltzmann constant.

The cloud and water vapor feedbacks are calculated as the change of CRF and GHE in response to the per unit degree of surface air temperature increase (Cess and Potter, 1988; Sun et al., 2003, 2006). These measures are different from the offline radiative transfer calculations (Cess et al., 1990; Zhang et al., 1994), in which the partial feedback can be truly obtained (Soden et al., 2004). These measures tend to overestimate (or underestimate) the feedback from the greenhouse effect of water vapor (or clouds) (Sun et al., 2006). However, since the feedbacks in the models are measured in the same way as those in observations, the results are still useful to understand the sources of model biases (Sun et al., 2006). Therefore, we used these measures to quantify feedbacks in this study. The level of uncertainty is represented by ± 1 standard error of the regression.

3. Results

In this section, we discuss the climate sensitivities and their attributions under the different forcings. Firstly, we examine the potential drift in the control run. Then, we calculate the model sensitivities to different external forcing agents. The physical processes that affect the model sensitivity are discussed with special focus on the cloud and water vapor responses.

3.1 *Energy balance and the drift in the control run*

The time series of TOA fluxes and SAT of the control run are shown in Figs. 1b–e. The magnitudes of the fluxes agree well with observations at the TOA. The mean absorbed solar radiation in the model is 232.5 W m^{-2}, which is in good agreement with ERBE data (234.0 W m^{-2}). The underestimation in the model is only 1.5 W m^{-2}. The TOA outgoing longwave radiation in the model is 229.6 W m^{-2}, which is about 4 W m^{-2} less than that derived from ERBE observations (234.0 W m^{-2}). The net energy bias at TOA is about 2.9 W m^{-2}. Although there exists a minor energy surplus, the outgoing longwave fluxes roughly compensate the incoming net shortwave fluxes at TOA.

In the pre-industrial control run, there is a cold SAT drift with a magnitude of about 0.2 K $(1000\ \text{yr})^{-1}$ Following the Stefan–Boltzmann equation, this drift trend of temperature corresponds to a trend of -0.16 W m^{-2} $(1000\ \text{yr})^{-1}$ in the outgoing longwave radiation. The corresponding drift in net TOA radiative flux is about 0.2 W m^{-2} $(1000\ \text{yr})^{-1}$. The effect of the long-term drift on last-millennium climate simulation will be discussed in the following analysis.

3.2 *Energy imbalance and climate sensitivities of the model*

The reproduction of three typical climate periods of the past millennium depends on the model's responses to the specified natural and anthropogenic forcings. The climate of the MWP and LIA represent changes in solar variability and volcanic eruptions, while the warming in the 20th century is dominated by increased anthropogenic GHG emissions (Crowley, 2000; Meehl et al., 2004; Zhou et al., 2011). Given the

different forcing mechanisms, we divide the entire millennium into two periods: the pre-industrial (before 1850 A.D.) and industrial (after 1850 A.D.) eras. The first period is dominated by natural forcings including solar variability and volcanic eruptions, while the second period forcings are dominated mainly by GHG as well as anthropogenic aerosol emissions. The effects of different forcing agents on the global mean energy balance at TOA in the millennial simulation are evident in Fig. 2. In the early stage prior to 1850, the specified effective solar radiation changes are reflected in the incoming shortwave radiation levels at TOA, with excessive input during the MWP period (1000 A.D.–1300 A.D.), but deficient input during the LIA period (1550 A.D.–1850 A.D.) (Fig. 2a). The anomalous incoming shortwave radiation is balanced by the outgoing longwave radiation (Fig. 2b). Thus, the perturbations of net radiation at TOA are small in the pre-industrial period (Fig. 2c).

The second period of last-millennium climate is dominated by a warming tendency associated with increasing anthropogenic forcing (GHG emissions and sulfate aerosols). The anthropogenic forcing, including GHGs in the industrial era (mainly the 20th century), impacts the climate system though either protecting or reducing the levels of outgoing infrared radiation. The perturbation of net radiation at TOA after 1850 is far greater than that in the pre-industrial period (Fig. 2c).

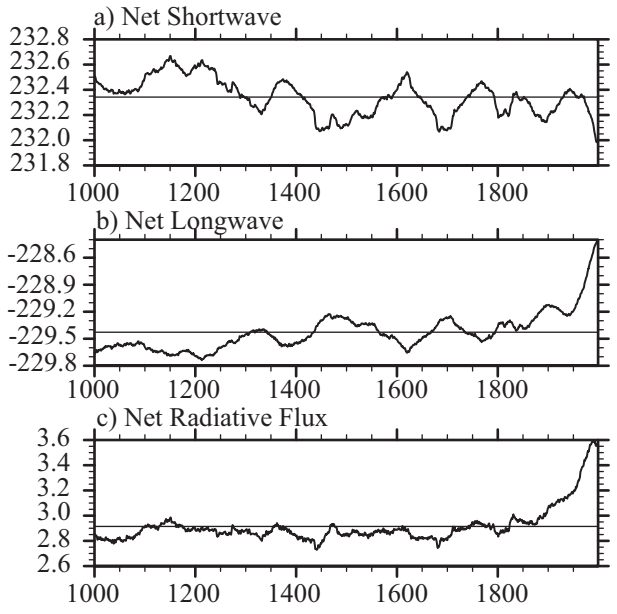

Fig. 2. Global mean energy balance at TOA in the last-millennium climate simulation: (a) net shortwave flux; (b) net longwave flux; (c) net radiative flux (downward is positive; units: W m^{-2}).

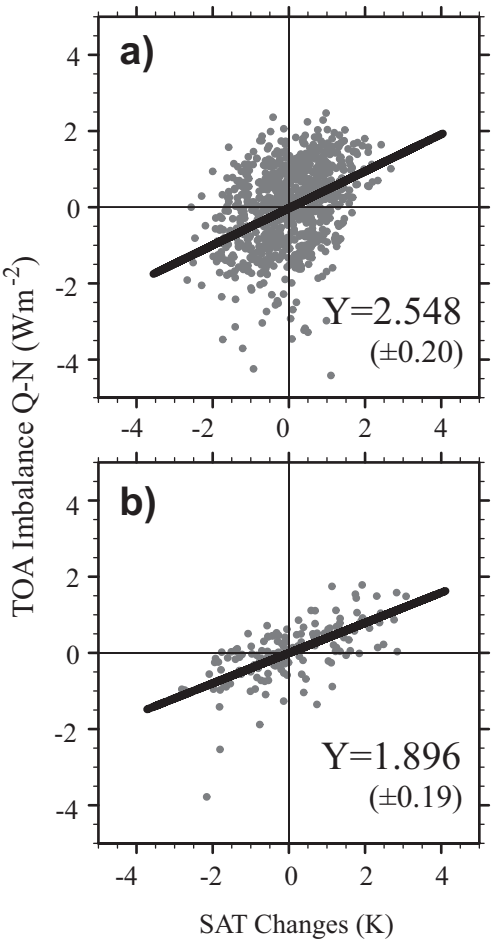

Fig. 3. Feedback term (Y; units: W m^{-2} K^{-1}; parentheses show the uncertainty) of FGOALS-gl: (a) pre-industrial period (before 1850 A.D.); (b) industrial period (after 1850 A.D.).

Based on Eq. (4), we estimated the system feedback factors for the pre-industrial era and the industrial era (Fig. 3). In the pre-industrial period, the feedback factor (Y) is 2.5 W m^{-2} K^{-1}, indicating that the model's climate sensitivity to natural forcing is 0.4 K (W m^{-2})$^{-1}$. In the industrial era, the feedback factor reduces to 1.9 W m^{-2} K^{-1}, indicating that the climate sensitivity increases to 0.5 K (W m^{-2})$^{-1}$.

The weak model sensitivity in the pre-industrial period results in a weak response of the model system to the specified effective solar radiation changes, and thus weak temperature anomalies during the MWP (Fig. 1a). The SAT difference between the MWP and LIA in the model is also weaker than the reconstruction (Fig. 1a). Given the weak sensitivity of the model to the specified effective solar radiation forcing in the pre-industrial era, a weaker-than-reconstruction LIA climate is hypothesized. However, the model still shows a reasonable performance in LIA simulation.

We suggest that the reasonable reproduction of the LIA climate is partly attributed to the climate drift of the coupled system. In the last-millennium simulation, the MWP (1000 A.D.–1300 A.D.) SAT is about 0.1°C warmer than in the LIA period (1550 A.D.–1850 A.D.) (Fig. 1a). In the 1000-yr pre-industrial control run, although no change in the effective solar radiation forcing is specified, the early stage (1000–1300 model years) is still 0.055°C warmer than the later stage (model years 1550–1850), indicating the internal climate drift has a contribution of 0.055°C to the entire 0.1°C warming in the all-forcing past-millennium climate simulations. In the industrial era, the strong model sensitivity offsets the cold drift and results in a reasonable simulation of SAT in the 20th century (Fig. 1a). In the all-forcing run, the 20th century (1900–2000) has a warmer SAT of 0.29°C relative to the millennial average. The SAT anomaly in the model is close to the reconstruction, which is about 0.17°C. In the 1000-yr pre-industrial control run, the SAT anomaly during model years 900–1000 is −0.03°C, indicating the internal climate drift makes a contribution of −0.03°C to the 0.29°C warming in the all-forcing run.

Why did the model show different climate sensitivity in the pre-industrial period and the industrial era? In the following section, we discuss the contributions of cloud and water vapor responses.

3.3 *Analysis of cloud responses*

3.3.1 *Evolution of cloud radiative forcing in the last-millennium simulation*

Cloud affects the Earth's climate via cloud radiation forcing. The SWCRF is negative and tends to cool the Earth system, while the LWCRF is positive and tends to warm it. The evolutions of CRF anomalies in the last-millennium simulation are shown in Fig. 4. The CRF generally tends to resist the specified forcing agents. The TOA energy budget indicates a weaker-(stronger)-than-normal SWCRF in the colder (warmer) climate periods. This phenomenon mainly reflects the effects of cloud optical depth and albedo changes. The year-by-year fluctuation of LWCRF is weaker than that of SWCRF in the last-millennium simulation, except for the 20th century. This difference is expected since the LWCRF is dominated by the responded outgoing infrared flux, which is small in the pre-industrial period due to the low concentration of GHGs. In the 20th century, the increased anthropogenic GHG levels reduce the clear-sky outgoing longwave radiation, which further results in negative LWCRF anomalies.

The CRF feedbacks derived from satellite datasets and the model are compared in Fig. 5. Note that the interannual variability has been removed by producing a 4-yr overlapping average. The ISCCP and CERES data are similar in their signs of feedback, although the uncertainties are somewhat large in CERES. Both of the observational datasets feature a positive LWCRF feedback (Fig. 5a), indicating that warmer conditions favor a stronger LWCRF, which may further amplify the initial warming by its greenhouse effect. In contrast, the SWCRF feedback is negative in the observations (Fig. 5b), indicating that in a warmer climate the strong solar cooling effects of clouds may cripple the initial warming. In the observations, these two effects compensate each other and finally result in a negative net cloud radiative feedback (Fig. 5c).

In the industrial era of the past-millennium simulation, both LWCRF and SWCRF feedbacks are negative, resulting in a negative net CRF feedback (Figs. 5g–i). The scatter plot shows that the SWCRF changes are not proportional to SAT variation in the model. These disproportional scatters are mainly evident in the period 1950–2000 A.D. After 1950 A.D., while the weak solar radiative forcing reduces the SWCRF, the enhanced anthropogenic forcing continues to heat the system and SAT (Fig. 5h). The hook-like pattern causes a huge level of uncertainty and reduces the mean SWCRF negative feedback of the

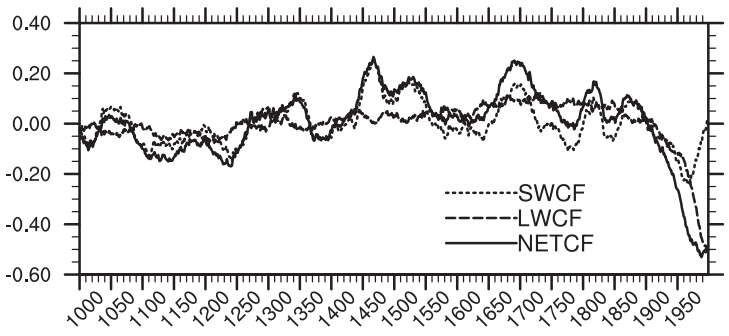

Fig. 4. Global mean CRF anomaly at TOA in the last-millennium climate simulation (upward is positive; units: W m^{-2}).

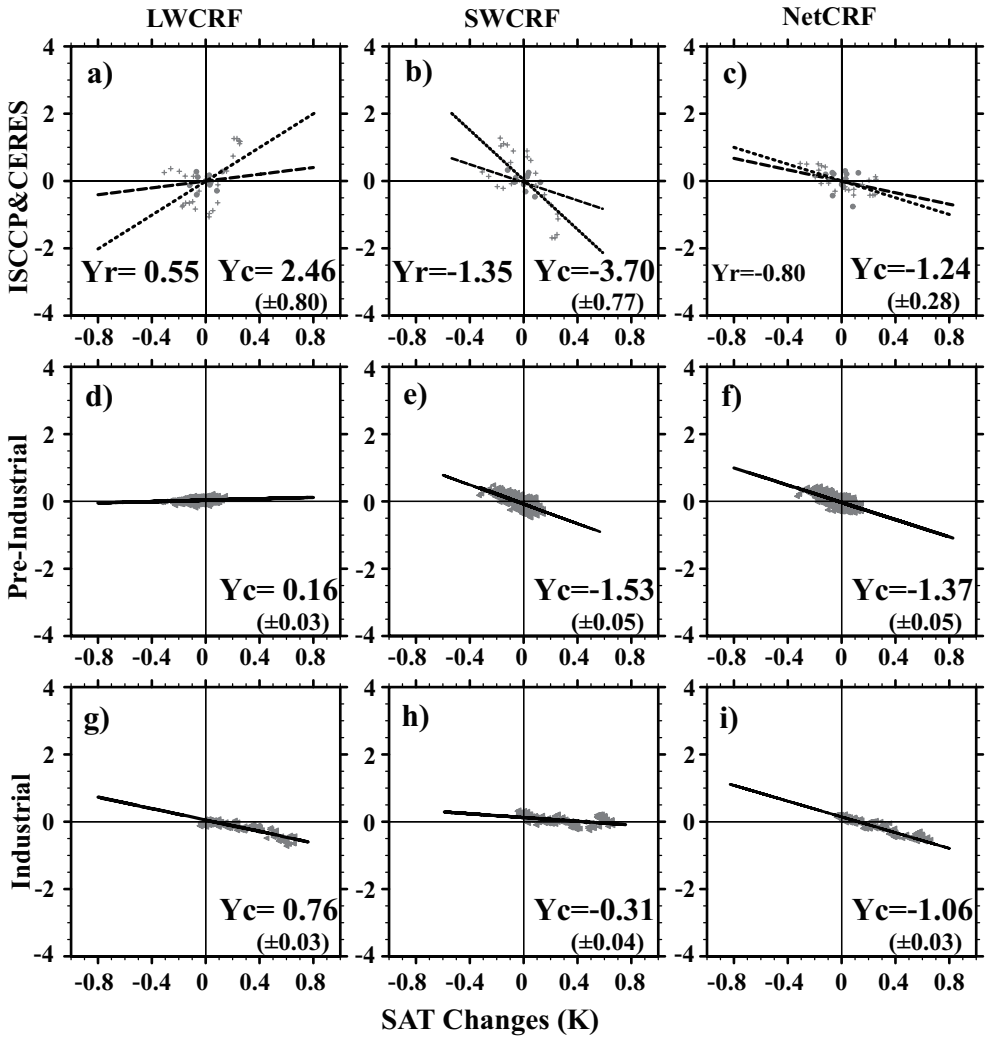

Fig. 5. Global mean SAT (x-axis; units: K) vs. CRF anomalies (y-axis; units: W m^{-2}): (a) LWCRF feedback; (b) SWCRF feedback; and (c) net CRF feedback in ISCCP (dotted lines with asterisks) and CERES data (dashed lines with dots); (d–f) and (g–i) are the same as (a–c), but for the simulated pre-industrial period and industrial period. Note: interannual variability has been removed; the numbers in the plots represent the magnitude of response; parentheses show the uncertainty.

whole industrial period. Thus, negative LWCRF feedback dominates net CRF feedback (Figs. 5g and i).

In the pre-industrial period, a negative SWCRF feedback can be seen (Fig. 5e), with a magnitude stronger than that of the industrial era. The most significant difference between the pre-industrial and industrial periods is the sign of LWCRF feedback, which is negative in the industrial era but uncertain in the pre-industrial era (Figs. 5d and g). Owing to the dominance of negative SWCRF feedback, the net CRF feedback is also negative during the pre-industrial period (Fig. 5f). In FGOALS-gl, such a type of negative net CRF feedback dominates the whole millennial simulation, suppresses the temperature responses, and thus acts as a negative forcing mechanism on the model sensitivity.

3.3.2 *Response of cloud properties*

As shown in Eqs. (1–3), the radiative fluxes are derived from the CWP, cloud fractions, effective radius of cloud particles, ice mixed ratio, and so on. To further understand the cloud radiative feedbacks and their changes, these elements were also checked in our study. Figure 6 shows the cloudiness and CWP responses derived from both ISCCP data and the simulation. An uncertain CWP response to SAT changes can be seen in the observational data (Fig. 6b). However, the simulated CWP response is positive and stronger

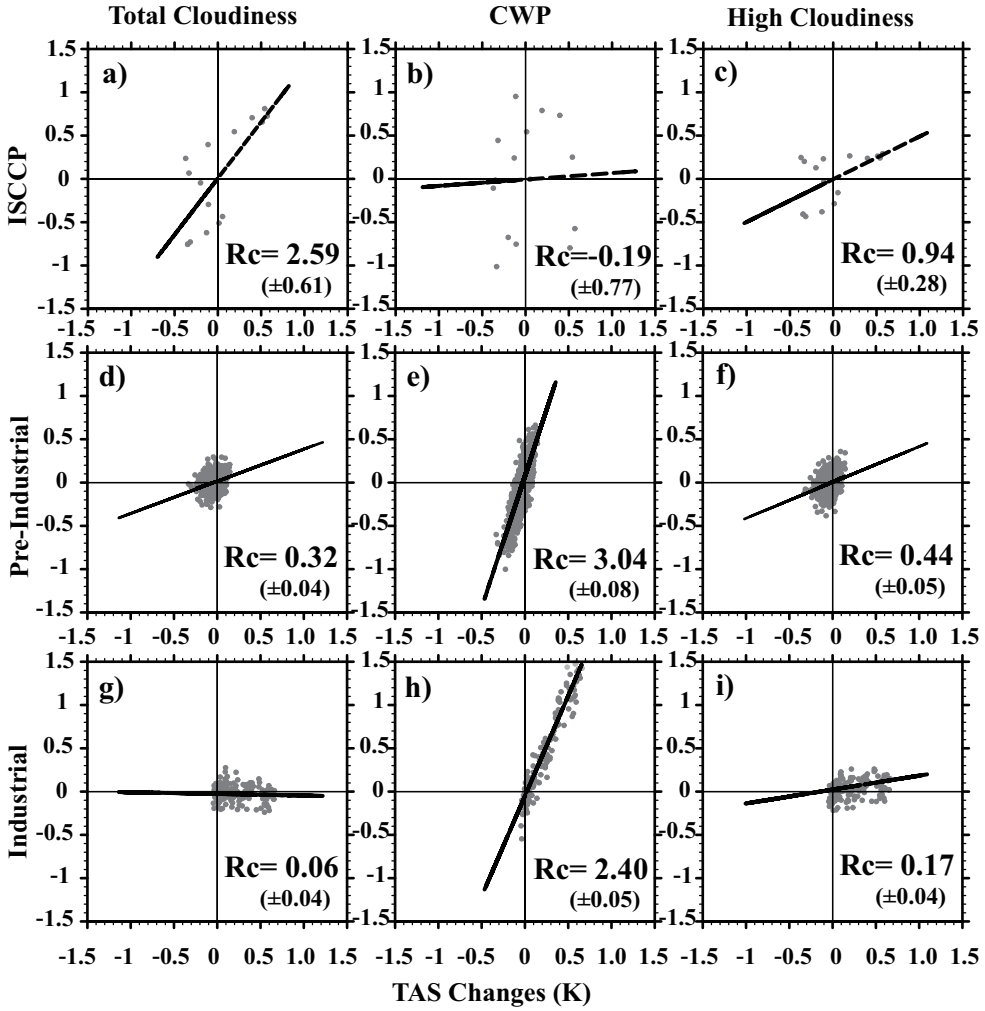

Fig. 6. Responses of cloud properties (y-axis) to SAT anomalies (x-axis; units: K): (a) total cloudiness response; (b) CWP response; and (c) high cloudiness response in ISCCP D2 data; (d–f) and (g–i) are the same as (a–c), but for the simulated pre-industrial period and industrial period. Note: interannual variability has been removed; the numbers in the plots represent the magnitude of response, parentheses show the uncertainty.

than observed (Fig. 6e). The CWP responses involve many physical processes, such as precipitation, convection, detrainment, and other microscale physical processes. The lifetime of convection in a warmer climate is always longer, and the conditions are wetter when compared to a colder climate. Both the longer lifetime of convection and the wetter conditions are conducive to cloud condensation (Zhang and Bretherton, 2008). Based on Eqs. (1) and (2), more CWP would lead to a stronger cloud optical depth and thereby higher emissivity and reflection. Such a type of positive CWP response further reinforces the CRFs. Because the SWCRF is more sensitive to CWP changes than LWCRF (Kiehl, 1994), the positive response of CWP tends to result in a positive LWCRF feedback but a stronger negative SWCRF feedback. Thus, the positive CWP response finally induces a negative net CRF feedback in FGOALS-gl.

In the observational data, the cloud fraction exhibits a positive response, mainly from the contribution of high cloud (Figs. 6a and c). Because the value of LWCRF increases with cloud height, while the value of SWCRF is not sensitive to cloud-top height (Kiehl, 1994), the increased high cloud leads to a positive LWCRF feedback and partly offsets the negative effect of CWP. In the observation, the CWP response is weak or almost uncertain (Fig. 6b), and the CRF feedback is dominated by the increased cloudiness, resulting finally in an uncertain net CRF feedback (Figs. 5a–c). However, the responses of cloud fraction, high cloud, and CWP in the model are far different to the observation (Fig. 6b). The disagreement is evident in both the pre-industrial period and the industrial era (Figs. 6d–f).

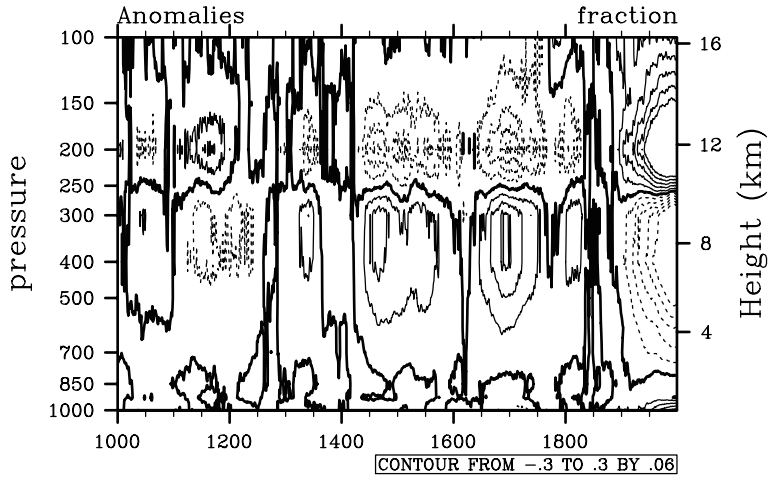

Fig. 7. Global mean variation of cloud anomalies in the last-millennium climate simulation (units: %). The thick black line is 0, and the dashed contours represent negative anomalies. The contour interval is 0.06%.

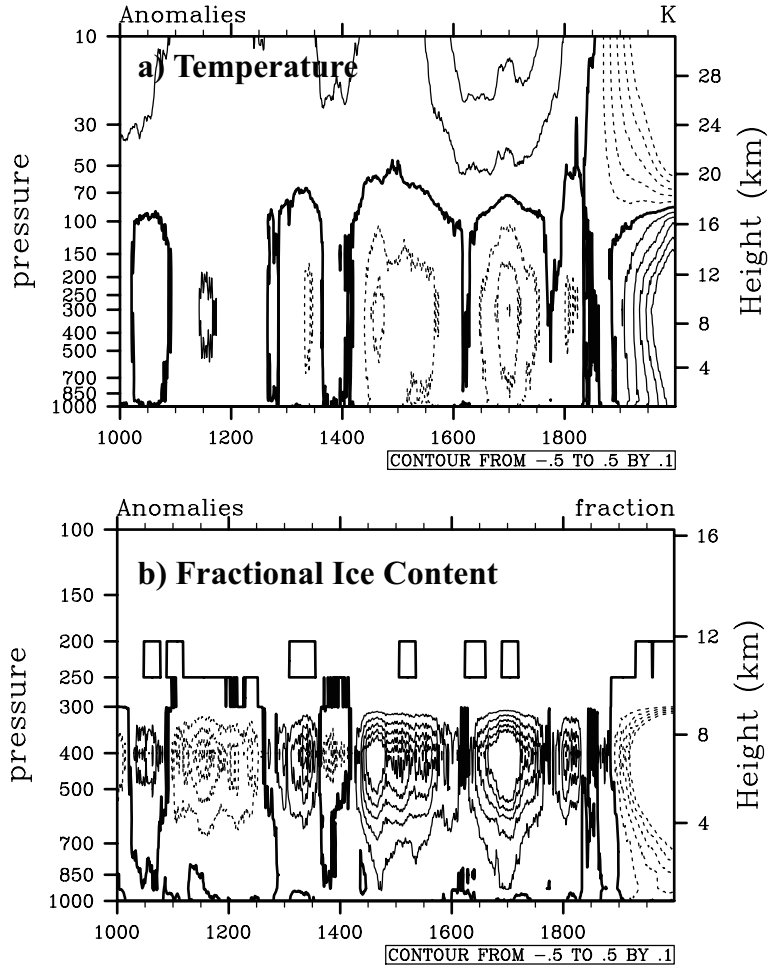

Fig. 8. Global mean variation of (a) temperature (units: K) and (b) fractional ice content within cloud (units: %) anomalies in the last-millennium climate simulation. The contour interval is 0.1 K in (a) and 0.1% in (b).

In order to further understand the cloudiness response, Fig. 7 is plotted to show the evolution of cloudiness anomalies at each level. A weak positive high cloud response can be seen throughout the whole millennial simulation. The high cloud changes might reflect the effect of deep convections (Wetherald and Manabe, 1988). In the warm stages, such as the MWP and 20th century, the increased high clouds prohibit more outgoing infrared radiation, and thus amplify the initial warming. Despite this effect, however, the change of high cloud is too weak (less than 0.5%, even in the 20th century) to offset the negative SWCRF feedback due to CWP change by inducing a positive LWCRF feedback. Since the CWP and optical depth are exponential to SWCRF (Kiehl, 1994), the CWP dominates the net CRF feedback and finally leads to a negative net CRF feedback. The negative feedback damps the initial temperature changes and reduces the climate sensitivity of the model, especially in the pre-industrial period.

In industrial period, the positive responses of high cloud and CWP are still evident. However, the expected positive LWCRF feedback is replaced by negative feedback (Figs. 5d and g), implying that other factors may compensate or even overwhelm the effects of cloudiness and CWP.

Figure 8a shows the vertical profile of temperature anomalies in the last-millennium simulation. In the warm period, a warm troposphere is always coupled with a cold stratosphere (Fig. 8a). In the Kristjánsson and Kristiansen (2000) cloud effective radius scheme, which is applied in FGOALS-gl, the effective radius of ice cloud drip is a function only of temperature. The warmer troposphere thus tends to result in a larger effective radius of ice particles. In addition, the warmer troposphere also reduces the ice mixed content ($f_{\rm ice}$) in the melt mixing layers, as shown in Fig. 8b. Based on Eqs. (1–3), a decrease of fractional ice content and an enlarged ice particle content of cloud would lead to a reduction of cloud emissivity and optical depth. This further weakens the LWCRF.

In the industrial period, the tropospheric warming is strong enough to compensate the effects of the CWP on LWCRF (Fig. 8a). Thus, as shown in Figs. 5d and e, there is a robust negative LWCRF but a weaker negative SWCRF feedback. As a result, the climate sensitivity becomes stronger in the industrial period, as shown in Fig. 3b.

Besides LWCRF, the well-known positive water vapor feedback (Cess et al., 1990; Zhang et al., 1994) is another process that can amplify the initial temperature change and make positive contributions to the climate sensitivity. The water vapor feedbacks derived from the observation and the simulation are compared in Fig. 9. The observation features a positive water vapor feedback (Fig. 9a). In the pre-industrial period, the positive water vapor feedback is 3.4 W m^{-2} K^{-1}, which is about 2.4 W m^{-2} K^{-1} less than the observed

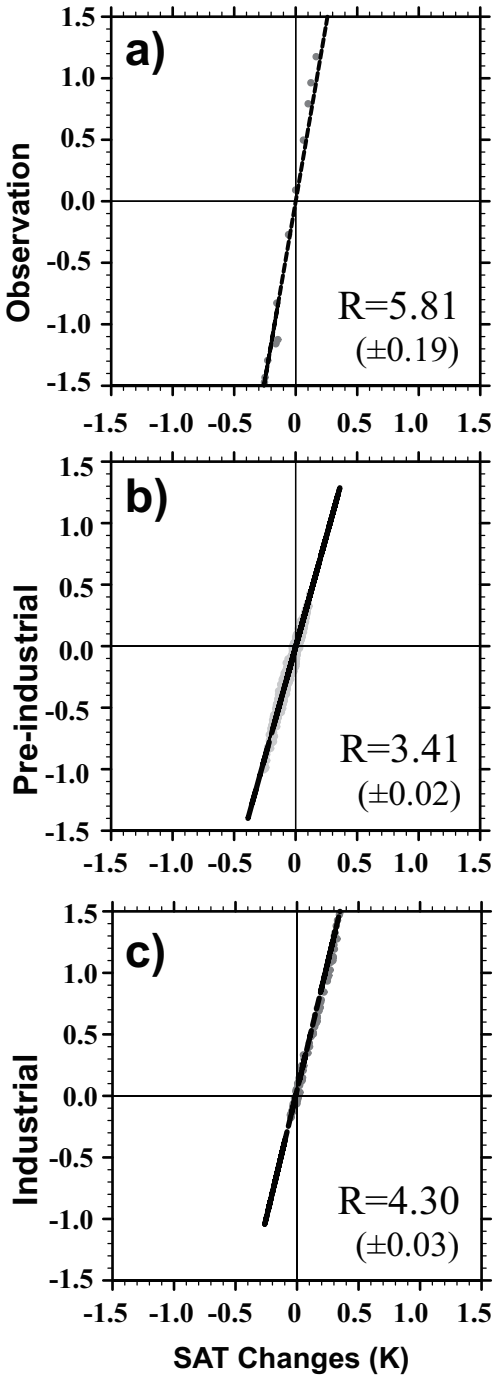

Fig. 9. Responses of greenhouse effects (y-axis) to SAT anomalies (x-axis; units: K) in (a) the observation; (b) pre-industrial period; and (c) industrial era. The numbers in the plots represent the magnitude of feedback (W m^{-2} K^{-1}); parentheses show the uncertainty.

value of about 5.8 W m^{-2} K^{-1} derived from ISCCP data (Fig. 9b). In the industrial period, the water vapor feedback is 4.3 W m^{-2} K^{-1}, which is still weaker than the observation but stronger than that of the pre-industrial period (Fig. 9c). The stronger water vapor feedback also favors higher model sensitivity in the industrial era.

Based on the above analysis, we conclude that both the negative cloud feedback and the weak positive water vapor feedback reduce the climate sensitivity of FGOALS-gl. Because the cloud (water vapor) feedback is weak (strong) in the industrial period, the model sensitivity during the industrial era is stronger than that in the pre-industrial period.

4. Summary

Last-millennium climate simulation by FGOALS-gl shows reasonable performance in its simulation of the LIA and 20th century warming, but a weak reproduction of the MWP. To understand the model's sensitivity to external and internal forcing agents, the energy balance, climate sensitivity and absorption feedback of the model were analyzed. The major results can be summarized as follows.

(1) The feedback factor of FGOALS-gl is 2.5 W m^{-2} K^{-1} in the pre-industrial period, reducing to 1.9 W m^{-2} K^{-1} in the industrial era. Thus, FGOALS-gl is more sensitive to anthropogenic forcing (mainly GHGs) than natural forcing. This was evidenced by the changes of climate sensitivity, which is 0.4 K $(W\ m^{-2})^{-1}$ during the pre-industrial period, but increases to 0.5 K $(W\ m^{-2})^{-1}$ during the industrial era.

(2) The weak model sensitivity in the pre-industrial period results in weak temperature anomalies during the MWP. The relatively reasonable reproduction of the LIA is partly attributed to the aforementioned model drift [approximately -0.055 K $(1000\ yr)^{-1}$] in the pre-industrial control run. In the industrial era, however, the higher-than-preindustrial-period model sensitivity overwhelms the cold drift and leads to a reasonable simulation of 20th century warming.

(3) Negative net cloud radiative forcing feedback and an underestimated positive water vapor feedback work through the whole past-millennium climate simulation of FGOALS-gl. Both of them reduce the model climate sensitivity. In the industrial era, however, the higher-than-preindustrial-period water vapor feedback and lower-than-preindustrial-period cloud feedback make the coupled system more sensitive to anthropogenic forcing (mainly GHGs) than natural forcing. This eventually leads to a reasonable simulation of 20th century warming.

(4) Analyses indicate that a strong positive CWP response dominates FGOALS-gl and favors a negative net cloud feedback, while a positive high cloud response is also evident in the last-millennium simulation and favors a positive LWCRF and cloud feedback. Because the cloud response is too weak to compensate the effect of CWP, the final effect is dominated by a negative cloud feedback, which reduces the model sensitivity. In the industrial era, the strong tropospheric temperature response enlarges the effective radius of ice clouds and reduces the fractional ice content within cloud, resulting in a reduction of cloud emissivity and optical depth. Both of these favor higher model sensitivity and thus a reasonable simulation of 20th century global warming.

Acknowledgements. This work was jointly supported by the "Strategic Priority Research Program—Climate Change: Carbon Budget and Related Issues" of the Chinese Academy of Sciences (Grant No. XDA05110301) and NSFC under Grant Nos. 40890054 and 41125017.

REFERENCES

Ammann, C. M., F. Joos, D. S. Schimel, B. L. Otto-Bliesner, and R. A. Tomas, 2007: Solar influence on climate during the past millennium: Results from transient simulations with the NCAR Climate System Model. *Proceedings of the National Academy of Sciences*, **104**, 3713–3718.

Barkstrom, B. R., and G. L. Smith, 1986: The earth radiation budget experiment—Science and implementation. *Rev. Geophys.*, **24**, 379–390.

Cess, R. D., and G. L. Potter, 1988: A methodology for understanding and intercomparing atmospheric climate feedback processes in general-circulation models. *J. Geophys. Res.*, **93**, 8305–8314.

Cess, R. D., and Coauthors, 1990: Intercomparison and interpretation of climate feedback processes in 19 atmospheric general circulation models. *J. Geophys. Res.*, **95**, 16601–16615.

Cess, R. D., and Coauthors, 1996: Cloud feedback in atmospheric general circulation models: An update. *J. Geophys. Res.*, **101D**, 12791–12794.

Collins, W. D., and Coauthors, 2003: Description of the NCAR community atmosphere model (CAM2). NCAR Tech. Notes, Climate and Global Dynamics Division Boulder, Colorado, 109–110.

Colman, R., 2003: A comparison of climate feedbacks in general circulation models. *Climate Dyn.*, **20**, 865–873.

Crowley, T. J., 2000: Causes of climate change over the past 1000 years. *Science*, **289**, 270–277.

Doutriaux-Boucher, M., and G. Sèze, 1998: Significant changes between the ISCCP C and D cloud climatologies. *Geophys. Res. Lett.*, **25**, 4193–4196.

Forster, P. M., and J. M. Gregory, 2006: The climate sensitivity and its components diagnosed from Earth Radiation Budget data. *J. Climate*, **19**, 39–52.

Forster, P. M., and K. E. Taylor, 2006: Climate forcings and climate sensitivities diagnosed from coupled climate model integrations. *J. Climate*, **19**, 6181–6194.

Gregory, J. M., and Coauthors, 2004: A new method for diagnosing radiative forcing and climate sensitivity. *Geophys. Res. Lett.*, **31**, L03205, doi: 10.1029/2003GL018747.

Harrison, E. F., P. Minnis, B. R. Barkstrom, V. Ramanathan, R. D. Cess, and G. Gibson, 1990: Seasonal variation of cloud radiative forcing derived from the earth radiation budget experiment. *J. Geophys. Res.*, **95**, 18687–18703.

Held, I. M., and B. J. Soden, 2000: Water vapor feedback and global warming. *Annual Review of Energy and the Environment*, **25**, 441–475.

Held, I. M., and B. J. Soden, 2006: Robust responses of the hydrological cycle to global warming. *J. Climate*, **19**, 5686–5698.

Houghton, J. T., G. J. Jenkins, and J. J. Ephraums, 1990: *Scientific Assessment of Climate Change*. Cambridge University Press, 365pp.

Houghton, J. T., Y. Ding, D. J. Griggs, M. Noguer, P. J. Linden, X. Dai, K. Maskell, and C. A. Johnson, 2001: *Climate Change 2001: The Scientific Basis*. Cambridge University Press, 881pp.

Jansen, E., and Coauthors, 2007: Palaeoclimate. *Climate Change 2007: The Physical Science Basis. Contribution of Working Group I to the Fourth Assessment Report of the Intergovernmental Panel on Climate Change*. Solomon et al., Eds., Cambridge University Press, 748–845.

Kiehl, J. T., 1994: On the observed near cancellation between longwave and shortwave cloud forcing in tropical regions. *J. Climate*, **7**(4), 559–565.

Kristjánsson, J. E., and J. Kristiansen, 2000: Impact of a new scheme for optical properties of ice crystals on climates of two GCMs. *J. Geophys. Res.*, **105**, 10063–10079.

Man, W. M., and T. J. Zhou, 2011: Forced response of atmospheric oscillations during the last millennium simulated by a climate system model. *Chinese Science Bulletin*, **56**, 3042–3052.

Man, W. M., T. J. Zhou, J. Zhang, C. Wu, and B. Wu, 2010a: The equilibrium response of LASG/IAP climate system model to prescribed external forcing of little ice age. *Chinese J. Atmos. Sci.*, **34**, 914–924. (in Chinese)

Man, W. M., T. J. Zhou, and L. X. Zhang, 2010b: The tropical Pacific interannual variability simulated by LASG/IAP climate system model FGOALS-gl. *Chinese J. Atmos. Sci.*, **34**, 1141–1154. (in Chinese)

Manabe, S., and R. T. Wetherald, 1967: Thermal equilibrium of the atmosphere with a given distribution of relative humidity. *J. Atmos. Sci.*, **24**, 241–259.

Meehl, G. A., W. M. Washington, C. Ammann, J. M. Arblaster, T. M. L. Wigley, and C. Tebaldi, 2004: Combination of natural and anthropogenic forcings and 20th century climate. *J. Climate*, **17**, 3721–3727.

Mann, M. E., Z. Zhang, S. Rutherford, R. Bradley, M. Hughes, D. Shindell, C. Ammann, G. Faluvegi and F. Ni, 2009: Global signatures and dynamical origins of the Little Ice Age and Medieval climate anomaly. *Science*, **326**, 1256–1260

Ramanathan, V., R. D. Cess, E. F. Harrison, P. Minnis, B. R. Barkstorm, E. Ahmad, and D. Hartmann, 1989: Cloud-radiative forcing and climate: Results from the earth radiation budget experiment. *Science*, **243**(4887), 57–63.

Slingo, A., 1989: A GCM parameterization for the shortwave radiative properties of water clouds. *J. Atmos. Sci.*, **46**, 1419–1427.

Soden, B. J., A. J. Broccoli, and R. S. Hemler, 2004: On the use of cloud forcing to estimate cloud feedbacks. *J. Climate*, **17**, 3661–3665.

Sun, D. Z., and Coauthors, 2003: On the Radiative and dynamical feedbacks over the equatorial cold-tongue. *J. Climate*, **16**, 2425–2432.

Sun, D. Z., and Coauthors, 2006: Radiative and dynamic feedbacks over the equatorial cold-tongue: Results from nine atmospheric GCMs. *J. Climate*, **19**, 4059–4074.

Taylor, K. E., R. J. Stouffer, and G. A. Meehl, 2012: An overview of CMIP5 and the experiment design. *Bull. Amer. Meteor. Soc.*, **93**, 485–498.

Wen, X., T. J. Zhou, S. Wang, B. Wang, H. Wan, and J. Li, 2007: Performance of a reconfigured atmospheric general circulation model at low resolution. *Adv. Atmos. Sci.*, **24**, 712–728, doi: 10.1007/s00376-007-0712-7.

Wetherald, R. T., and S. Manabe, 1988: Cloud feedback processes in general circulation models. *J. Atmos. Sci.*, **45**, 1397–1415.

Zhang, J., 2010: General features of climate changes during the last 1000 years in a climate system model. Dissertation for the Doctoral Degree. Paris: L'Universite Pierre et Marie Curie, 8–9.

Zhang, J., T. J. Zhou, W. M. Man, and Z. Li, 2009: The transient simulation of little ice age by LASG/IAP climate system model. *Quaternary Sciences*, **29**, 1125–1134. (in Chinese)

Zhang, M., and C. Bretherton, 2008: Mechanisms of low cloud–climate feedback in idealized single-column simulations with the community atmospheric model, version 3 (CAM3). *J. Climate*, **21**, 4859–4878.

Zhang, M., J. J. Hack, J. T. Kiehl, and R. D. Cess, 1994: Diagnostic study of climate feedback processes in atmospheric general circulation models. *J. Geophys. Res.*, **99**, 5525–5537.

Zhang, Y., W. B. Rossow, A. A. Lacis, V. Oinas, and M. Mishchenko, 2004: Calculation of radiative fluxes from the surface to top of atmosphere based on ISCCP and other global data sets: Refinements of the radiative transfer model and the input data. *J. Geophys. Res.*, **109**, doi: 1029/2003JD004457.

Zhou, T. J., and R. C. Yu, 2006: Twentieth century sur-

face air temperature over China and the globe simulated by coupled climate models. *J. Climate*, **19**(22), 5843–5858.

Zhou, T. J., B. Wu, X. Y. Wen, L. J. Li, and B. Wang, 2008: A fast version of LASG/IAP climate system model and its 1000-year control integration. *Adv. Atmos. Sci.*, **25**, 655–672, doi: 10.1007/s00376-008-0655-7.

Zhou, T. J., B. Li, W. M. Man, L. X. Zhang, and J. Zhang, 2011: A comparison of the medieval warm period, the little ice age and the 20th century warming simulated by FGOALS climate system model. *Chinese Science Bulletin*, **56**, 3028–3041.